World Electric Vehicle Journal

MDPI

Article

State-of-Charge Balancing Control for Dual-Bus Battery System with Low-Voltage Output Regulation

Daxing Zhang [1], Xiangdong Wang [1], Yankai Wang [1], Bingzi Cai [1], Shisen Gao [1], Mingming Tian [1], Suxiong Cai [1], Yuehui Deng [1], Yuan Cao [2] and Feiliang Li [2,*]

[1] China Southern Power Grid Huizhou Power Supply Bureau, Huizhou 516000, China; wangyankai@gdhz.csg.cn (Y.W.); tianmingming@gdhz.csg.cn (M.T.)
[2] Department of Electrical Engineering, School of Automation, Central South University, 982 South Lushan Rd., Changsha 410083, China; ycao19@crimson.ua.edu
* Correspondence: 214606008@csu.edu.cn

Abstract: This article introduces a new method for balancing the state of charge (SOC) in a dual-bus battery system architecture. The system consists of multiple battery cells or modules connected in series to provide high voltage output. Additionally, low-power flyback converters are connected in series with each battery cell or module at the inputs, and their outputs are connected in parallel to provide lower voltage output. The SOC balancing algorithm ensures that the lower voltage output remains at a desired reference value by adjusting the average duty cycle of each power converter, while also balancing the rate of charge or discharge of each battery cell or module. This SOC balancing process does not affect the normal operation of the high voltage power output. In other words, the dual output (high voltage and low voltage) of the battery system can function independently, and the balancing current only flows through the low voltage power path. Experimental results from a prototype are provided and discussed to validate the proposed dual-bus battery system and controller.

Keywords: battery energy storage system; SOC balancing; flyback converter; lithium-ion battery

Citation: Zhang, D.; Wang, X.; Wang, Y.; Cai, B.; Gao, S.; Tian, M.; Cai, S.; Deng, Y.; Cao, Y.; Li, F. State-of-Charge Balancing Control for Dual-Bus Battery System with Low-Voltage Output Regulation. *World Electr. Veh. J.* **2024**, *15*, 10. https://doi.org/10.3390/wevj15010010

Academic Editor: Carlo Villante

Received: 23 November 2023
Revised: 12 December 2023
Accepted: 19 December 2023
Published: 27 December 2023

1. Introduction

In recent years, the development of the smart grid philosophy and proactive integration of renewable energies such as wind and solar power into the power grid have led to increased research into energy storage systems. One of the most commonly used systems is the lithium-ion battery energy storage system, which offers advantages such as a long cycle life, high energy density, and high reliability [1–8]. According to the different cathode materials, lithium-ion batteries can be divided into a lithium cobalt oxide (LCO) battery, lithium manganese oxide (LMO) battery, lithium iron phosphate (LFP) battery, and ternary material lithium battery [9]. They are widely used in consumer electronics, electric vehicles, and other energy storage scenarios due to their unique characteristics.

Due to individual battery cells with a low voltage and capacity, series or parallel connections of multiple cells are used to meet the energy demands [10–17]. However, the battery cells may have mismatches due to the imperfection in the manufacturing process, operation condition, and self-discharge at different rates and wire and connector losses [18,19]. This could cause the charge imbalance in the lithium-ion battery. The imbalances can result in overcharging and over-discharging [20,21]. While improvements to manufacturing can help ensure the batteries are the same at the start, deviations can still occur during operation. Therefore, SOC balancing technology is necessary to address these imbalances.

Battery SOC balancing can be classified into passive balancing and active balancing based on the energy transfer mode during the balancing process as shown in Figure 1. Passive balancing involves shunting the strongest cells in a battery pack with a dissipative

element [22,23]; therefore, the energy transfer occurs through resistive heating, which leads to a low balancing current and slow balancing speed.

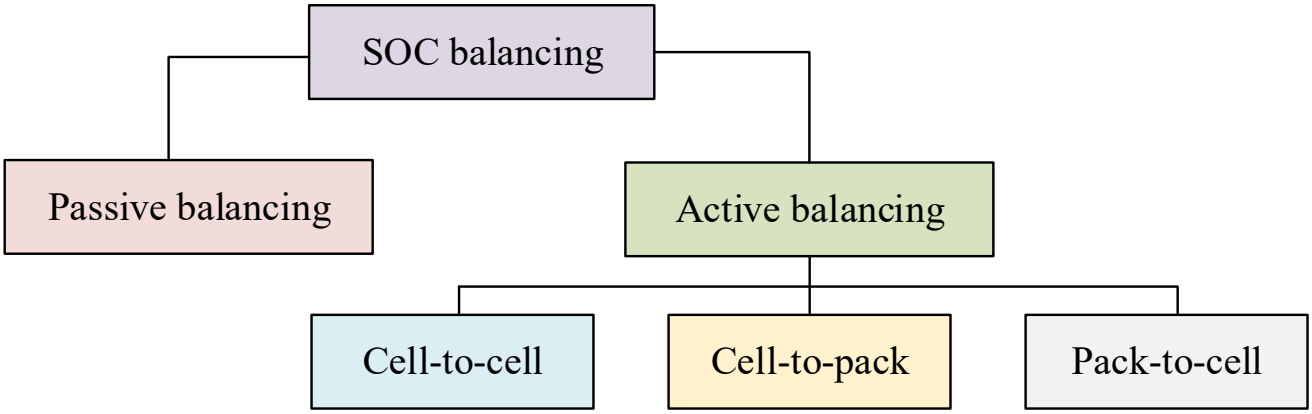

Figure 1. Classification of SOC balancing.

On the other hand, active balancing involves the transfer of energy between batteries with different SOC, allowing for a higher balancing current and thus achieving faster balancing speeds. Since there is no resistive heating (neglecting wire losses), active balancing achieves higher efficiency. It can be seen that active balancing is crucial for battery systems as it can improve efficiency, prolong battery life, and enhance safety. It is an important function of battery management systems. And active balancing can be classified into several types: Cell-to-cell [24], Cell-to-pack [25], and Pack-to-cell [26]. In the Cell-to-cell method, SOC balancing can be achieved through energy transferring between the specific cells. The Cell-to-pack method discharges the cell with the highest SOC to the entire battery pack or string. In contrast, in the Pack-to-cell method, the entire battery string energy is used to charge the cell with the lowest SOC.

Various topologies have been proposed to implement balancing, including methods that use capacitors, power converters, transformers, and combined elements [23–35]. The basic balancing architecture involves connecting capacitors in parallel to each cell for energy transfer [24], but it can only achieve active balancing between adjacent batteries. An additional row of capacitors can be added to achieve balance between any batteries [27]; however, these methods often suffer from slow balancing speed. A method to achieve fast equilibrium is to adopt a single high-power equalization circuit that is connected to the battery unit to be adjusted through a switch [28–31]. However, this approach is limited to processing one cell at a time, leaving other cells to continue to diverge, which can be time-consuming for large series battery packs.

To speed up the equalization process, a hierarchical structure can be constructed, which is divided into two layers for control of the bottom and the top layer, respectively [32]. This, however, requires an increase in the component and complexity. The use of a multi-winding transformer can achieve the synchronous balancing of a battery pack, using fewer components [33,34]. However, the practical implementation of this approach may face obstacles, such as cost and difficulties in manufacturing transformers. Building a distributed battery system with power converters is a valid alternative for balancing control. In [35], a hierarchical SOC balancing controller is proposed based on a single-inductor multi-input single output power converter, demonstrating the ability to balance the SOC between multiple parallel and series-connected battery systems while maintaining the bus voltage. This approach offers improved balancing control with reduced complexity.

When batteries are applied to the EVs, a high-voltage (HV) bus is required for propulsion, and an LV bus (such as 12 V) for auxiliary loads is also necessary, such as instrumentation, lighting, etc. The balancing topologies presented in the previous literature [21–35] lack the ability to deal with the scenario to supply power to the loads of two different voltage levels, and an additional step-down power converter is commonly required. Figure 2a

shows the general active balancing structure for EVs, and the circuit is used to transfer energy. Here, an additional DC-DC is used for voltage step-down-wise to supply the low-voltage (LV) load. The challenges are the cost, efficiency, and size of the system. An alternative to the design is a serial-input–parallel-output (SIPO) architecture as shown in Figure 2b. In the SIPO battery system, the power converters are connected in series to each battery in the battery string, while the output of the converters is connected in parallel, which can supply power for HV and LV loads at the same time without an additional step-down converter. In [36], an SOC balancing strategy is proposed based on the SIPO structure using an isolated dual active bridge (DAB) converter, but the drawback is that the LV output is not controlled to be stable, and the design and cost of the DAB converter is complex and high.

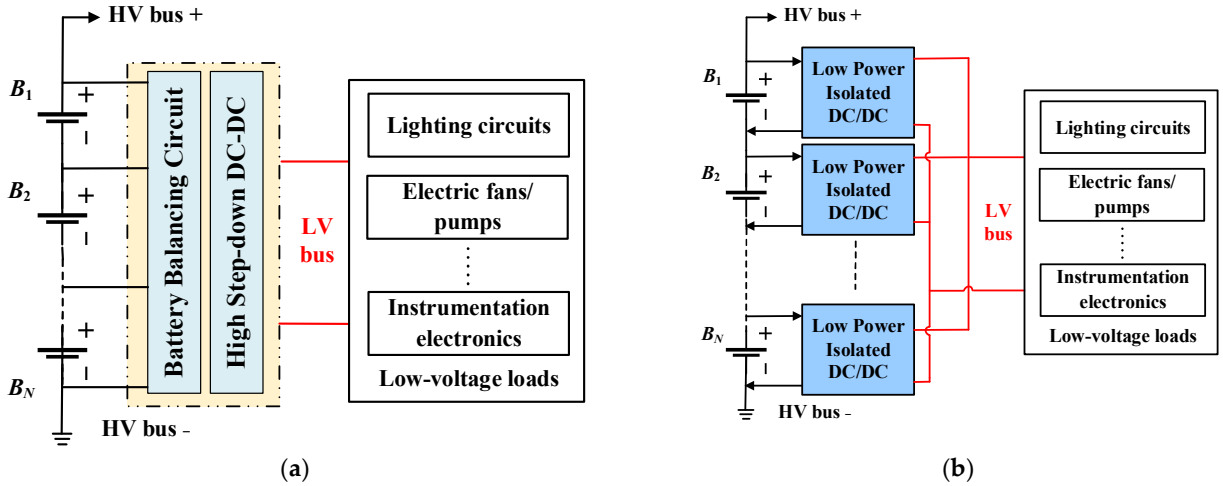

Figure 2. Illustration of battery system with SOC balancing circuit. (**a**) The general active balancing structure. (**b**) Serial-input–parallel-output balancing architecture.

To achieve SOC balancing in a cost-effective and efficient manner, this article presents a simplified SOC active balancing structure that takes into account factors such as complexity, size, and cost. The key contributions of this article are as follows:

(1) An innovative dual-bus battery system is presented, which incorporates flyback converters and an SOC balancing controller. The proposed system setup enables effective SOC balancing while also ensuring a stable low-voltage output.
(2) To optimize performance, the system incorporates voltage control, SOC control, and current control loops. Additionally, the phase shift of the duty cycle control timeline is utilized to minimize output voltage ripple.
(3) The experimental results are showcased to assess and confirm the effectiveness of the system control during different discharging operations and cyclic charging–discharging operations.

Table 1 shows a comparison between this paper and previous works based on switching converters in [31,33,34,36]. Firstly, the dual-bus battery system presented in this paper outperforms [31,33,34] in terms of achieving high and low voltage outputs simultaneously. Moreover, compared to [36], the presented system is capable of achieving low-voltage regulation and utilizes significantly fewer switches (2N vs. 8N). Last but not least, the system's modularity is also a key advantage. The voltage stress of each converter remains constant regardless of the number of battery cells, making expansion simpler and more efficient.

The rest of this article is organized as follows: Section 2 presents the basic architecture of the battery system. Section 3 presents the operation principle of the system balancing controller. The small-signal modeling of the control algorithm is presented in Section 4. Sample experimental results are presented and discussed in Section 5. Section 6 concludes this article.

Table 1. Comparison with previous works.

	[31]	[33]	[34]	[36]	**This Work**
Voltage output	LV bus	HV bus	HV bus	Dual-bus	Dual-bus
Output voltage regulation	Yes	No	Yes	No	Yes
Switch (for N cells)	4N + 1	2N	1	8N	2N
Diode (for N cells)	0	0	N	0	0
Inductor (for N cells)	1	N	0	0	0
Coil winding (for N cells)	0	N	N + 1	2N	2N
Cost	Small	Medium	Small	High	Medium
Overall size	Small	Large	Small	Large	Medium
Speed	Medium	Slow	Medium	Fast	Fast

2. Architecture of Presented Battery System

The presented battery system's architecture diagram is shown in Figure 2b, while Figure 3 displays the circuit schematic of the proposed system. To create this system, flyback converters are used, which are commonly employed in low-power settings. This converter type was chosen due to its low cost and simple design when compared to DAB converters. In the system, each battery cell is connected in parallel with a single low-power flyback converter bypass. This converter is directly connected to the battery cell, and the outputs of all the converters are then connected in parallel to power the low-power load, such as lighting and instrumentation. The high-voltage loads of the system are powered directly by the series battery pack.

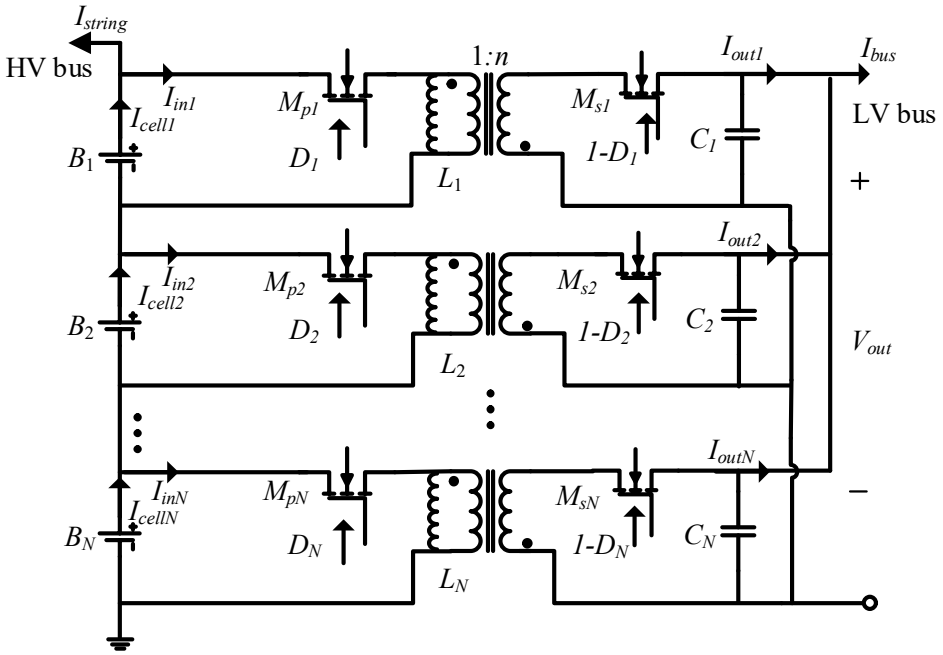

Figure 3. The circuit schematic of the presented system.

It is worth noting that in Figure 3, an ideal voltage source is used as the equivalent circuit of the battery. However, the actual equivalent circuit of a battery is quite complex due to its internal intricate electrochemical reactions. Typically, a second-order RC network is used to represent the equivalent circuit of a battery as shown in Figure 4. U_{OC} represents the open circuit voltage (OCV) of the battery, and refers to the voltage value of the battery when there is no load or current passing through it. It is a commonly used method to measure the battery and estimate its SOC. R_0 represents the ohmic resistance; R_1 and R_2 represent the polarization internal resistance, and C_1 and C_2 represent the polarization capacitance; V_O represents the terminal voltage of the battery. Nevertheless, the choice of

the equivalent circuit model does not affect the implementation of presented SOC balancing algorithms.

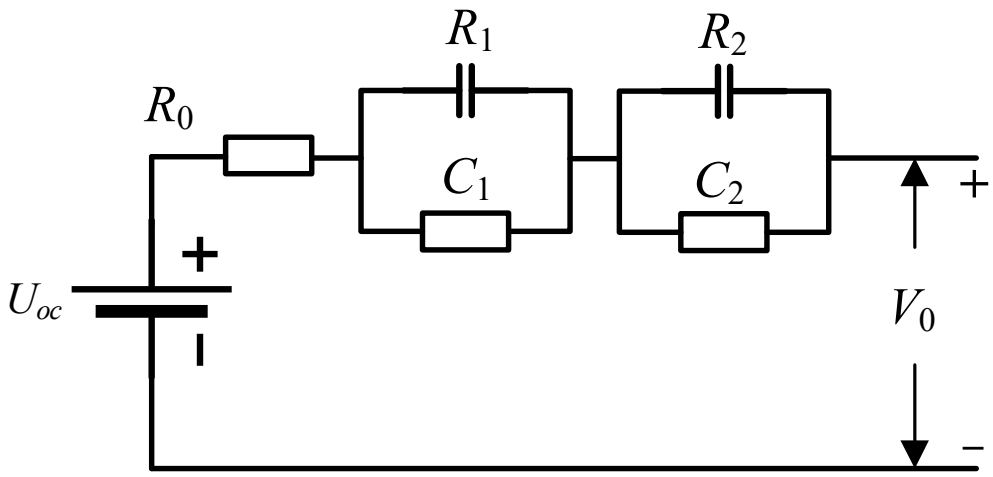

Figure 4. The second-order RC equivalent circuit model of lithium battery.

In the system, the current and voltage information are sensed to the controller, and the outputs of the controller are control signals (duty cycle D) to the converter. The converters are operated independently by using the LV output voltage V_{out} as the common voltage reference in a similar distributed operation, and the difference is that the battery cells are directly connected. And in the actual analysis and design of the flyback converter transformer, it can be regarded as a single magnetizing with an inductance L, as shown in Figure 5.

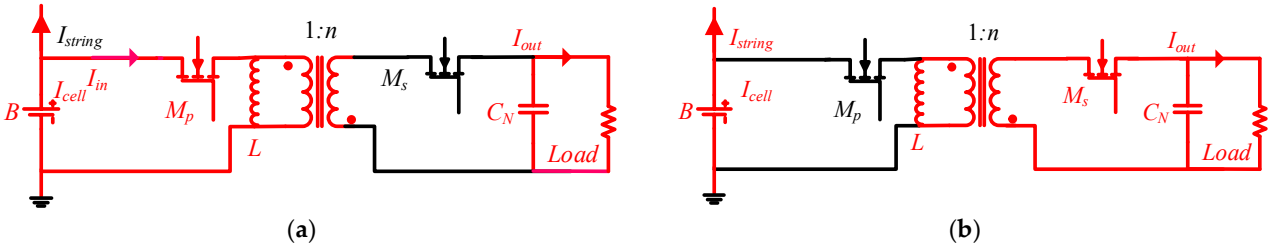

Figure 5. The operation equivalent circuit. (**a**) State I. (**b**) State II.

Each flyback converter implementation process in the presented system can be divided into two operation states—state I and state II—during one Pulse Width Modulation (PWM) cycle.

In state I, the switch M_p turns on and M_s turns off, as illustrated in Figure 3a. During this state, the battery cell provides power to the inductor L, and the balancing current I_{in} is generated. Meanwhile, the load connected to the secondary windings is powered by the energy stored in the capacitor.

In state II, the switch M_p turns off and M_s turns on, as shown in Figure 3b. During this state, the primary circuit is disconnected, and the energy stored in the transformer is transferred to the load.

3. The Operation Principle of the System Balancing Controller

This section focuses on the discussion of the system control, which realizes SOC balancing, voltage, and current stability at the same time. Figure 6 shows a battery pack consisting of N series cells with the controller. The controller mainly includes three control parts: the voltage loop, the SOC balancing algorithm, and the current loop. The basic concepts of the proposed SOC balancing are that by designing and adjusting the voltage loop, current loop, and SOC loop, and adjusting the duty cycle of each converter, the

charging/discharging current of each battery can be independently controlled. For example, for a battery with a high SOC, the corresponding control loop will output a larger power converter duty cycle to achieve a larger output current, and vice versa.

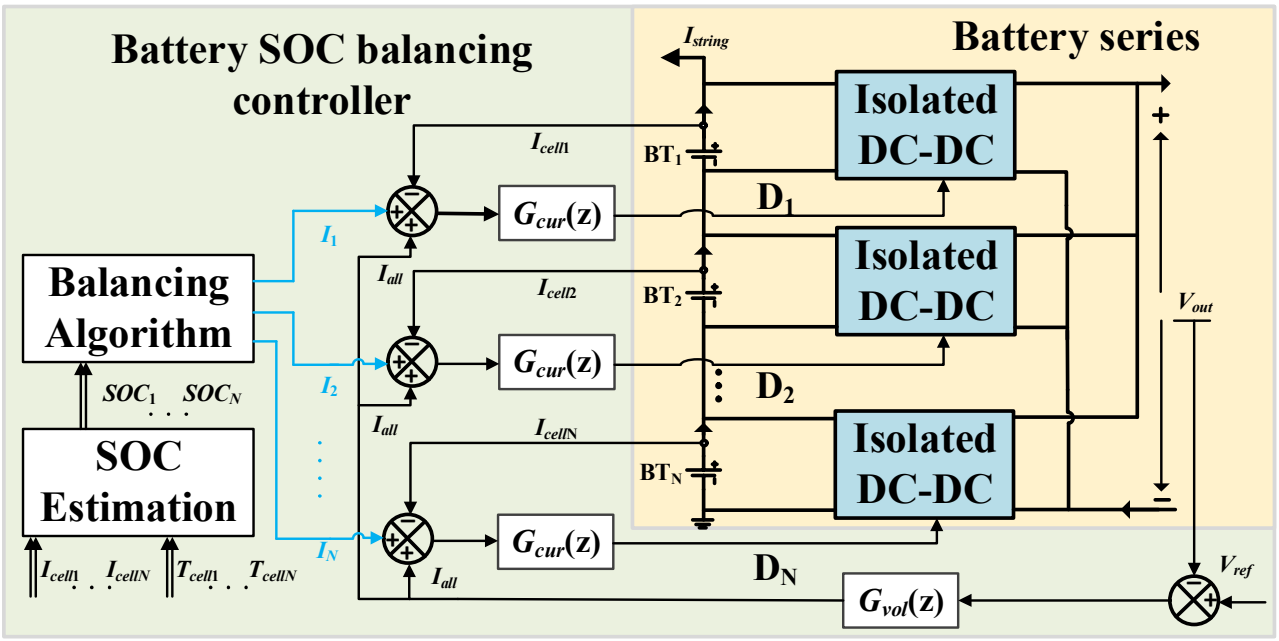

Figure 6. The block diagram of the proposed controller.

In the experimental setup's voltage control loop, the output voltage (V_{out}) is compared with a reference voltage (V_{ref}). Any difference between these two voltages is then sent to a digital proportional–integral (PI) compensator ($G_{vol}(z)$), as shown by Equation (1), which is responsible for ensuring that the voltage stays at the desired level. The PI compensator has two parameters, K_{p_vol} and K_{i_vol}, which determine the proportional and integral gains, respectively. The voltage compensator's output (I_{all}) is then used as the common current input reference in the current control loop, as given by Equation (2).

$$G_{vol}(z) = K_{P\_vol} + \frac{K_{I\_vol} \times z}{z - 1} \tag{1}$$

$$I_{all} = \left(V_{ref} - V_{out}\right) \cdot G_{vol}(z) \tag{2}$$

The system's balancing algorithm uses individual current variation references to achieve SOC balancing among the N cells. The SOC values are calculated using the combination of the coulomb counting method and OCV method in this article. Equation (3) is the basic principle of coulomb counting and demonstrates how the SOC value is calculated using the start time (t_0) and end time (t_1) of the SOC calculation interval, the battery cell's capacity (Q_{cell}), the discharging/charging current (I_{cell}, positive for discharging and negative for charging), and the initial SOC value (SOC_0). This equation takes into account the amount of charge (current multiplied by time) that has either been added to or withdrawn from the battery cell in order to accurately determine the SOC value. In order to calculate SOC_0, the OCV-SOC curve of the battery is measured in this paper as shown in Figure 7. When the battery is under working operation, coulomb counting is utilized for real-time SOC calculation. Meanwhile, when the battery is under rest, OCV is utilized for SOC initial estimation and calibration.

$$SOC = SOC_0 - \int_{t_0}^{t_1} \frac{I_{cell}}{Q_{cell}} dt \tag{3}$$

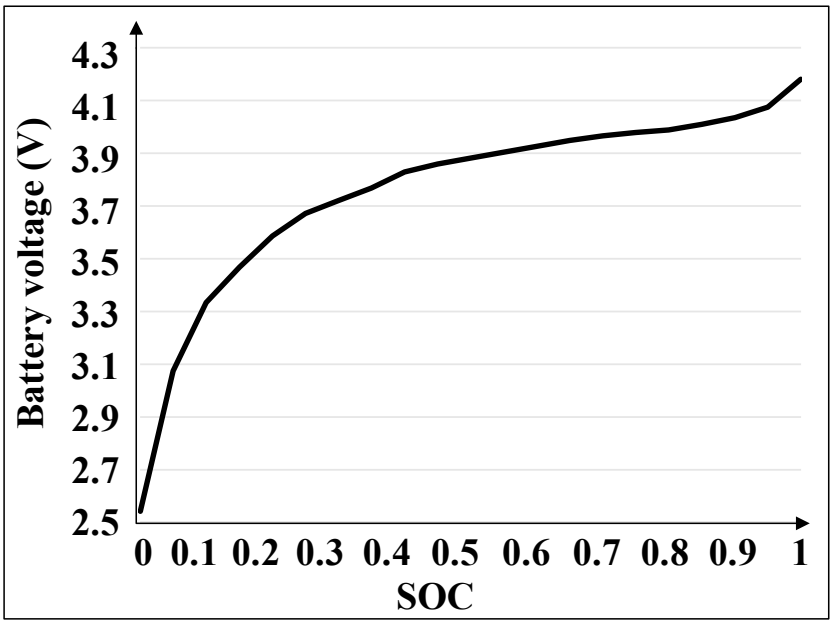

Figure 7. The OCV-SOC curve of the battery.

Figure 8 displays the block diagram of the balancing algorithm. The SOC compensator receives as input the difference between the *SOC* value of the cell and the reference value SOC_{ref}. SOC_{ref} is obtained by averaging the *SOC* values of all cells according to Equation (4). N represents the number of series battery cells. The individual current variation references (I_1 through I_N) are the outputs of the balancing algorithm. These references are converted to the current control section, as represented in Equation (5). The transfer function of the digital SOC balancing compensator, denoted as $G_{soc}(z)$, is given by Equation (6).

$$SOC_{ref} = \frac{1}{N}\sum_{i=1}^{N}(SOC_1 + SOC_2 + \cdots + SOC_i) \tag{4}$$

$$\begin{cases} I_1 = 1 - (SOC_{ref} - SOC_1)G_{soc}(z) \\ I_2 = 1 - (SOC_{ref} - SOC_2)G_{soc}(z) \\ \cdots\cdots \\ I_N = 1 - (SOC_{ref} - SOC_N)G_{soc}(z) \end{cases} \tag{5}$$

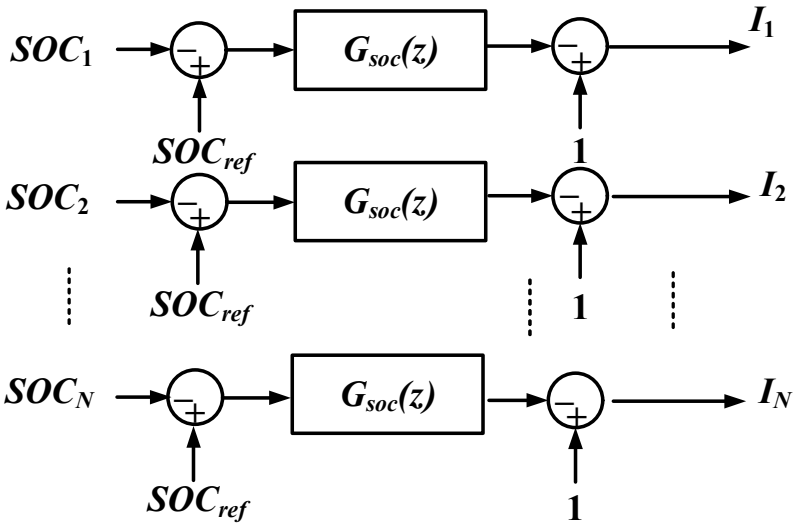

Figure 8. The block diagram of the balancing algorithm.

In the current control loop, the total input current reference of the ith cell I_{refi} is established, which is obtained by adding the common current reference I_{all} and the current variation reference I_i as given by Equation (7). The difference between the total input current reference current I_{refi} and battery cell discharge current I_{celli} as given by Equation (8), where I_{string} is the current of the HV bus and I_{bai} is the input current of the ith converter, is utilized as the input of the current compensator G_{cur} (z) as given by Equation (9), and the duty cycles for the flyback converters are obtained as given by Equation (10).

$$I_{refi} = I_{all} + I_i \tag{6}$$

$$I_{celli} = I_{string} + I_{ini} \tag{7}$$

$$G_{cur}(z) = K_{P\_cur} + \frac{K_{I\_cur} \times z}{z-1} \tag{8}$$

$$\begin{cases} D_1 = (I_{ref1} - I_{cell1})G_{cur}(z) \\ D_2 = (I_{ref2} - I_{cell2})G_{cur}(z) \\ \cdots\cdots \\ D_N = (I_{refN} - I_{cellN})G_{cur}(z) \end{cases} \tag{9}$$

It can be observed that the battery cell with a higher *SOC* value will be controlled to operate on a higher duty cycle and provide a greater portion of the power to the load compared to a battery cell with a lower *SOC* value. This mechanism results in the *SOC* values of multiple cells moving closer to each other. At a steady state, the output voltage of all the converters is equal to the expected reference voltage (V_{ref}). At equilibrium, the current variation references for all the N cells are identical, and the discharge current of the cells is the same.

4. The Small-Signal Modeling of the Control Algorithm

System stable operation is the premise of system control. Thus, the stability of the proposed structure is essential. Developing a system model is critical for the control design. Small-signal modeling is a proper approach for developing a linear transfer function for the desired operating conditions.

4.1. Small-Signal Model for the Converter

The small-signal ac and quiescent value equations of the flyback converter are derived from study [37] as given by Equations (10) and (11):

$$\begin{gathered} 0 = DV_g - D'\frac{V}{n} - DR_{on}I \\ 0 = \left(\frac{D'I}{n} - \frac{V}{R}\right) \\ I_g = DI \end{gathered} \tag{10}$$

$$\begin{gathered} L\frac{d\hat{i}(t)}{dt} = D\hat{v}_g(t) - D'\frac{\hat{v}(t)}{n} + \left(V_g + \frac{V}{n} - IR_{on}\right)\hat{d}(t) - DR_{on}\hat{i}(t) \\ C\frac{d\hat{v}(t)}{dt} = \frac{D'\hat{i}(t)}{n} - \frac{\hat{v}(t)}{R} - \frac{I\hat{d}(t)}{n} \\ \hat{i}_g(t) = D\hat{i}(t) + I\hat{d}(t) \end{gathered} \tag{11}$$

where R_{on} and R are the resistance of the MOSFET and output load. For given quiescent values of input voltage V_g, duty cycle D (D' = 1 − D), and turn radio n, the system of output voltage V, transformer equivalent inductor current I, and input current I_g can be found. In Equation (11), ˆ denotes the perturbed values in Equation (10). Taking the Laplace transform of Equation (11) to derive the transfer function, assuming the initial conditions are zero, as given by Equation (12)

$$\begin{gathered} sL\hat{i}(s) = D\hat{v}_g(s) - D'\frac{\hat{v}(s)}{n} + \left(V_g + \frac{V}{n} - IR_{on}\right)\hat{d}(s) - DR_{on}\hat{i}(s) \\ sC\hat{v}(s) = \frac{D'\hat{i}(s)}{n} - \frac{\hat{v}(s)}{R} - \frac{I\hat{d}(s)}{n} \\ \hat{i}_g(s) = D\hat{i}(s) + I\hat{d}(s) \end{gathered} \tag{12}$$

By eliminating $\hat{i}(s)$ and setting $\hat{v}_g(s)$ to zero, and assuming that the MOSFET is ideal, the resistance Ron is considered to be zero. The transfer function of the flyback converter's output voltage $\hat{v}(s)$ to its duty cycle $\hat{d}(s)$, denoted as $G_{vdr}(s)$, can be solved as Equation (13). Similarly, the transfer function of the flyback converter's input current $\hat{i}_g(s)$ to its duty cycle $\hat{d}(s)$, denoted as $G_{idr}(s)$, can be derived as Equation (14).

$$G_{vdr}(s) = \frac{-nILRs + nRV_g}{n^2LRCs^2 + n^2Ls + D'^2R} \tag{13}$$

$$G_{idr}(s) = \frac{-n^2DILs + n^2DV_g}{n^2D'LRCs^2 + n^2D'Ls + D'^3R} \tag{14}$$

4.2. Small-Signal Model for the Proposed Battery System

Based on the control block diagrams shown in Figure 7 in Section 3, the small-signal model diagram of the system loops is shown in Figure 9. L_{vol}, L_{curi}, and L_{soci} are loop gain transfer functions of the voltage, current, and SOC control loop, respectively, which can be derived as given by Equations (15) through (17), where H_{vol} and H_{cur} are the gains of the voltage sensor and current sensor, and G_{pwm} is the PWM modulator gain. $ZOH_{vol}(s)$, $ZOH_{cur}(s)$, and $ZOH_{soc}(s)$ are the zero-order-hold transfer functions as given by Equations (18) through (20), and T_{vol}, T_{cur}, and T_{soc} are the sampling times of the voltage, current, and SOC value. $G_{i\text{-}soc}$ is the transfer function of the cell current to SOC value as given by Equation (21), and Q_{cell} is the capacity of the cell. The values for these system parameters, which are used in the experiment, are provided in Table 2.

$$L_{vol}(z) = Z\{G_{vdr}(s) \cdot H_{vol} \cdot ZOH_{vol}(s)\} \cdot G_{vol}(z) \tag{15}$$

$$L_{curi}(z) = Z\{G_{pwm} \cdot G_{id}(s) \cdot H_{cur} \cdot ZOH_{cur}(s)\} \cdot G_{cur}(z) \tag{16}$$

$$L_{soci} = Z\{G_{i-soc} \cdot ZOH_{soc}(s)\}G_{soc}(z) \tag{17}$$

$$ZOH_{vol}(s) = (1 - e^{-s \cdot T_{vol}})/s \tag{18}$$

$$ZOH_{cur}(s) = (1 - e^{-s \cdot T_{cur}})/s \tag{19}$$

$$ZOH_{soc}(s) = (1 - e^{-s \cdot T_{soc}})/s \tag{20}$$

$$G_{i-soc} = \frac{T_{soc}}{Q_{cell}} \tag{21}$$

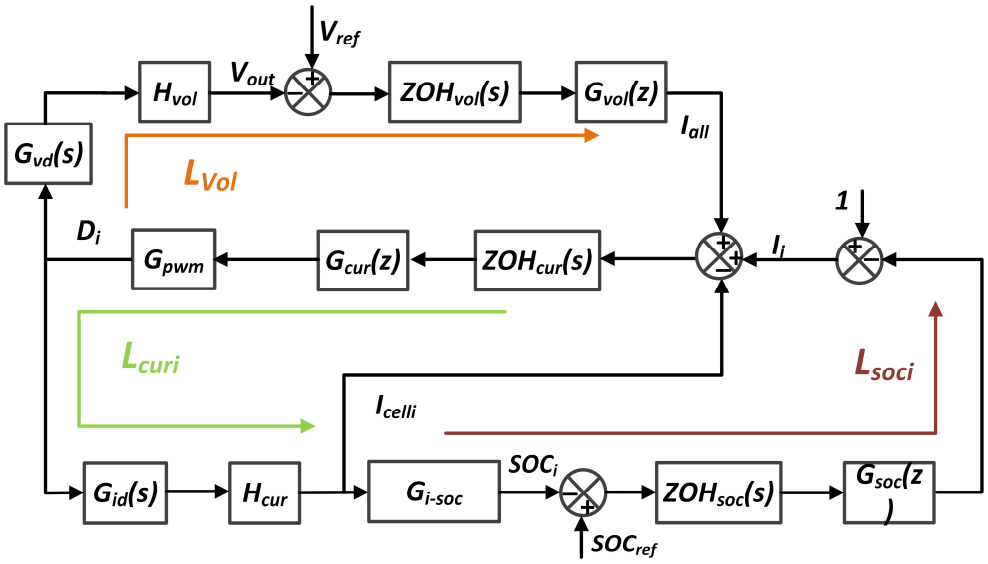

Figure 9. Small-signal model diagram of the system.

Table 2. Design parameters for the system control.

Parameters	Values	Parameters	Values
L	22 µH	n	1:1
C	220 µF	f	150 kHz
Q_{cell}	2 Ah	V_{celli}	3.7 V
V_{out}	8 V	I_{out}	2.5 A
H_{vol}	3 V/V	H_{cur}	0.132 V/A
T_{vol}, T_{cur}	5 µs	T_{soc}	1 s
K_{p_vol}/K_{p_cur}	0.51	K_{I_vol}/K_{I_cur}	0.5
K_{p_soc}	15.54	K_{I_soc}	15

5. Proof-of-Concept Experimental Prototype Results

In this laboratory section, a scale-down version of the four-cell battery system is tested to validate and assess its performance as illustrated in Figure 10. And the battery used in the experiments is the Panasonic NCR18650 battery. It is a lithium polymer battery with a positive electrode material of lithium nickel cobalt manganese oxide (Li (NiCoMn) O_2), which has a rated capacity of 2 Ah and a rated voltage of 3.7 V. To implement the control algorithm as described in Section 3, a TMS320F28335 floating-point micro-controller from Texas Instruments Inc. (Dallas, TX, USA) is utilized. This micro-controller offers 16 ADC channels and 12 PWM channels, meeting the experiment's needs.

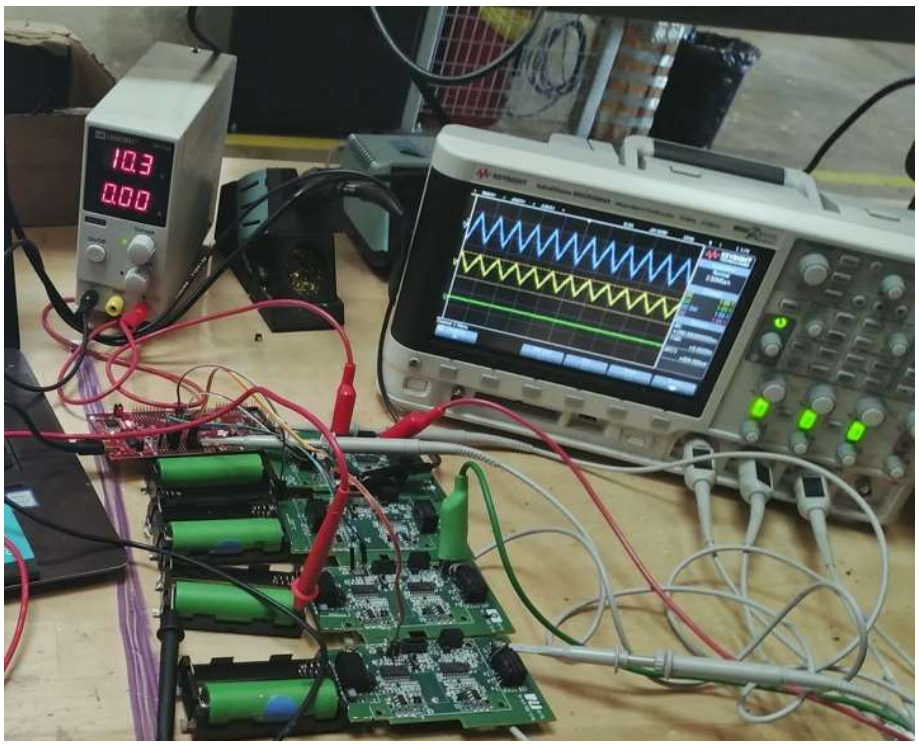

Figure 10. The experimental setup of the proof-of-concept experimental prototype.

5.1. Experimental Results When I_{string} Is Equal to Zero

When the discharge current of the main circuit of the battery pack is zero, the EV is parking. In this case, the I_{string} is equal to zero, but the low voltage power supply still works (the balancing circuit still works). In the proof-of-concept prototype experiment, the parallel output voltage of the power converter is regulated at 8 V with a 2.5 A output load current.

In order to evaluate the performance of the battery system and controller starting from the imbalanced SOC condition, the four cells are purposely made with different initial *SOC*

values of SOC_1 = 83%, SOC_2 = 79%, SOC_3 = 73%, and SOC_4 = 71%, and the maximum difference of the SOC values is ΔSOC_{max} = 12%. At the beginning, the reference SOC value $SOC_{ref} = (SOC_1 + SOC_2 + SOC_3 + SOC_4)/4$ = 76.5%. Therefore, the SOC balancing algorithm is activated and detects that the SOC values of cell1 and cell2 are larger than SOC_{ref}, and that the SOC value of cell3 and cell4 is smaller than SOC_{ref}. Under the action of the balancing algorithm, the current variation references expect that $I_1 > I_2 > I_3 > I_4$. Because each common input current reference I_{all} is the same, each current reference of the current loop expects that $I_{ref1} > I_{ref2} > I_{ref3} > I_{ref4}$. As a result, the discharge current of cell1 is the largest, followed by cell2, cell3, and cell4, until SOC balancing is achieved and $I_1 = I_2 = I_3 = I_4$.

Figure 11 shows the sample experimental results for the four-cell system during I_{string} = 0. Figure 11a,b show that cell1 has the largest current variation reference and the largest discharging current (the discharging current is positive and charging current is negative), while cell4 has the smallest current variation reference and the smallest discharging current. Therefore, cell4 and cell3 have a lower discharging rate (cell4 discharging slower than cell3), while cell2 and cell1 have a relatively higher discharging rate (cell1 discharging faster than cell2). The discharging behavior of the battery cells matches with the previous discussion and analysis. In this way, the SOC values of the four cells gradually become closer to each other through time until the SOC balancing is realized, and the current variation references are equal to one and maintained.

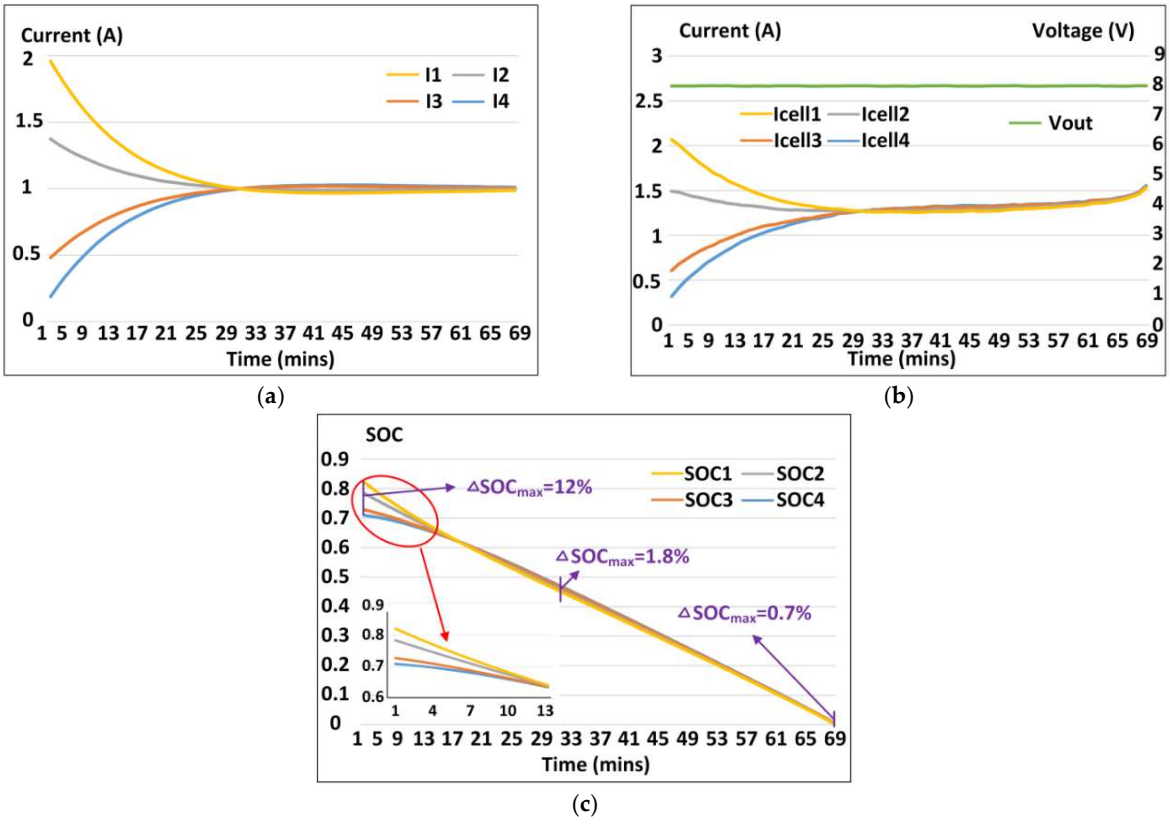

Figure 11. The sample experimental results when I_{string} is equal to zero. (**a**) The current variation references of the four cells. (**b**) The discharging currents of the four cells and the output voltage of the converters. (**c**) The SOC values of the four cells.

It should be noted that the current variation references (I_1 through I_4) are not exactly equal to one when the SOC balancing is realized as shown in Figure 11a. That is because the flyback converters used are not exactly symmetrical due to nonuniform PCB traces (parasitic). It can be observed from Figure 11b that the discharging currents of the cells tend to increase after SOC balancing, and ramp up at a faster rate at the end of the discharging

operation. The reason for this is that the terminal voltage of the cell decreases during the discharging, and more current is needed from the cell to satisfy the desired power.

Figure 11c shows the real-time *SOC* values of the four cells. As the discharge operation progresses, it can be seen that the *SOC* values of all four batteries begin to decrease. Since SOC_4 is the highest, it drops the fastest under the presented algorithm, and the SOC of all four batteries are almost the same at t = 13min and Table 3 records the specific numerical changes in four *SOC* values for the first 15 min. When t = 30 min, the *SOC* values of the four battery cells reach the balanced state and remain at the state until the end of the discharging. Under the continuous effect of the balance algorithm, the maximum difference is only 0.7%. It is also shown in Figure 11b that the parallel output voltage of the convert is always regulated at 8 V during the discharging as expected.

Table 3. Numerical changes in four SOC values.

Time/min	SOC_1	SOC_2	SOC_3	SOC_4	ΔSOC_{max}
1	0.8208	0.7839	0.7276	0.7091	0.1117
2	0.8031	0.7708	0.7220	0.7059	0.0972
3	0.7862	0.7582	0.7159	0.7020	0.0842
4	0.7697	0.7457	0.7094	0.6974	0.0722
5	0.7539	0.7336	0.7026	0.6924	0.0615
6	0.7383	0.7213	0.6952	0.6866	0.0517
7	0.7236	0.7095	0.6876	0.6806	0.0429
8	0.7089	0.6974	0.6797	0.6739	0.0349
9	0.6949	0.6857	0.6715	0.6670	0.0279
10	0.6810	0.6740	0.6630	0.6596	0.0214
11	0.6677	0.6626	0.6544	0.6519	0.0158
12	0.6544	0.6510	0.6454	0.6437	0.0107
13	0.6416	0.6398	0.6363	0.6353	0.0063
14	0.6290	0.6284	0.6270	0.6265	0.0024
15	0.6167	0.6172	0.6176	0.6177	0.0010

In order to evaluate the impact of different PI parameters on SOC balancing, additional experiments are conducted with different PI parameters. Three sets of PI parameters are shown in Table 4, and the experimental results are shown in Figure 12. It can be seen that as the gain of the PI parameters increases, the time for battery balancing decreases. However, the battery current may exhibit oscillations, as shown in Figure 12c. This is because a higher gain value for PI control leads to a faster response of the closed-loop system, but a faster SOC balancing controller speed may result in system response oscillations. Therefore, when designing controllers, there is a trade-off between the system response speed and stability, and suitable parameters need to be chosen.

Table 4. Different control parameters for the results of Figure 12.

Figures	K_{p_soc}	K_{I_soc}
Figure 12a	5.54	5.5
Figure 12b	15.54	15.0
Figure 12c	20.54	18.5

In practical application, load switching is very common. In order to further evaluate the performance of the battery system, a 2.5 A–1 A–3 A load current transient is applied at the output. As shown in Figure 13, the load transient of 2.5 A–1 A is triggered at t = 35 min, and the load transient of 1 A–3 A is triggered at t = 50 min. The SOC values of the four cells can achieve and maintain balancing until the end of the discharging not affected by the load transients, and the output voltage is always regulated at 8 V.

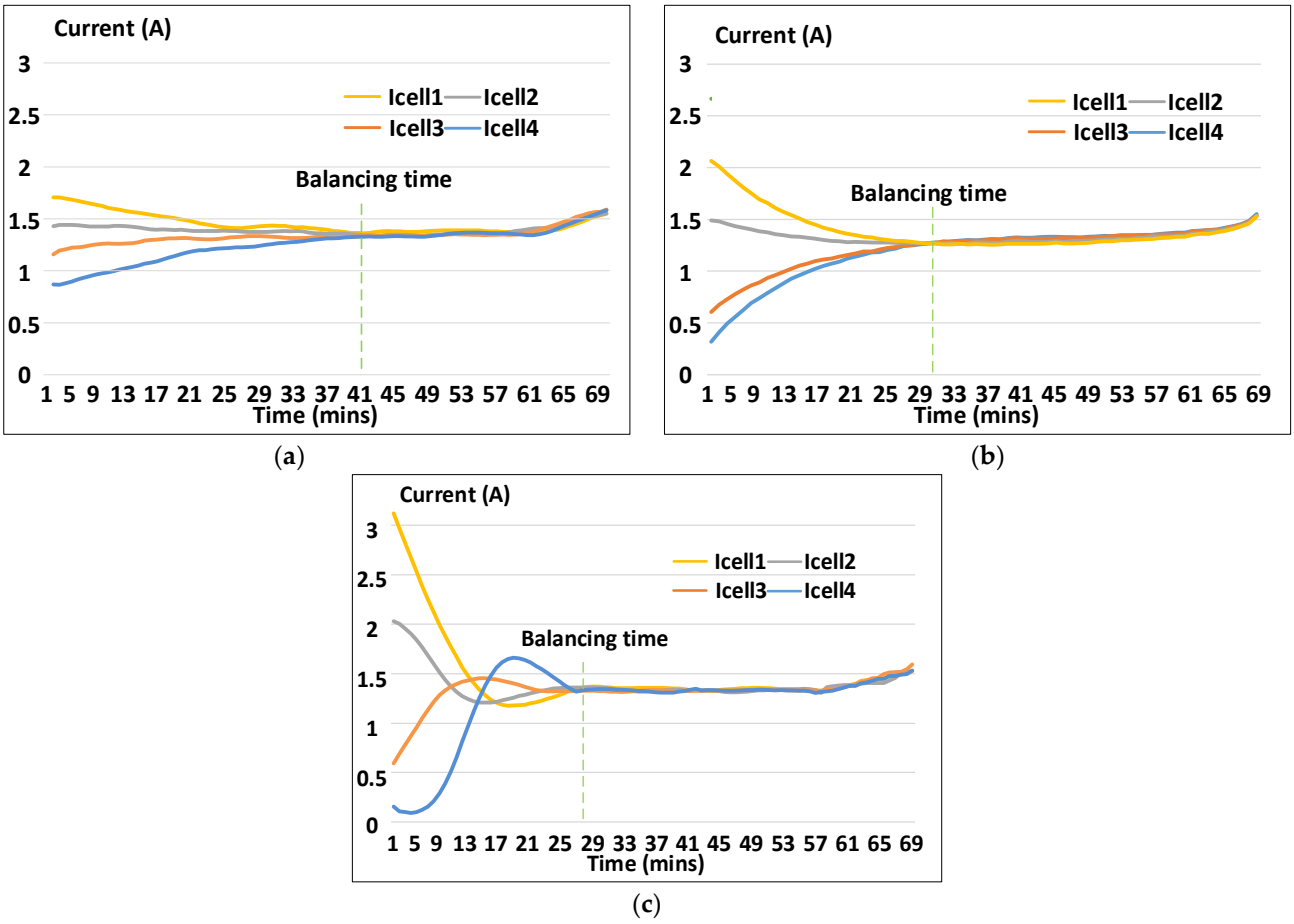

Figure 12. The discharging currents with different control parameters. (**a**) K_{p_soc} = 5.54 and K_{I_soc} = 5.5. (**b**) K_{p_soc} = 15.54 and K_{I_soc} = 15.0. (**c**) K_{p_soc} = 20.54 and K_{I_soc} = 18.5.

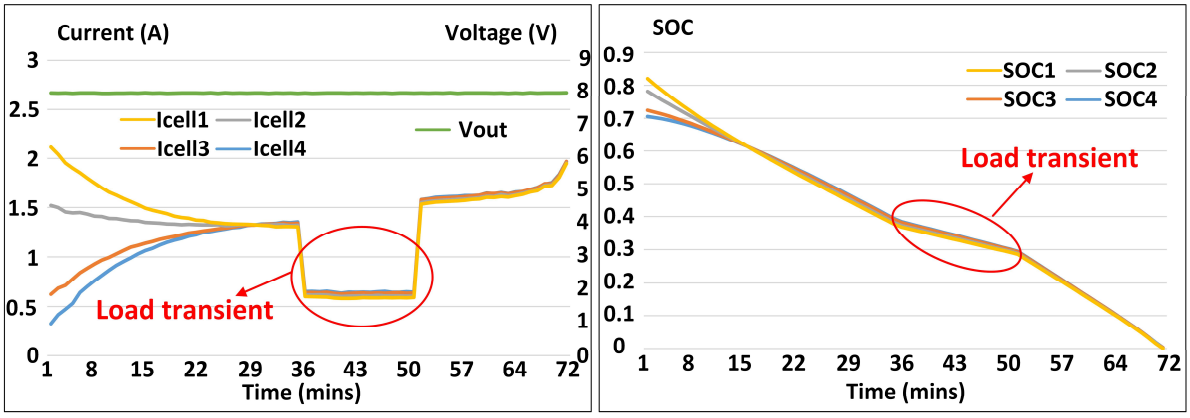

Figure 13. The sample experimental results when I_{string} is equal to zero with a load transient. (**a**) The discharging currents of the four cells and the output voltage of the converters. (**b**) The *SOC* values of the four cells.

5.2. Experimental Results When I_{string} Is Not Equal to Zero

In this section, the four-cell battery system supplies power to the main circuit and low-voltage load circuit (the balancing circuit) at the same time. In this case, the I_{string} is not equal to zero. In the experimental design, the main circuit discharges at 1 coulomb (equivalent to 2 A current according to the datasheet), and the parallel output voltage of

the power converter is regulated at 8 V with a 1 A output load current. The initial SOC values of the four cells are SOC_1 = 100%, SOC_2 = 97%, SOC_3 = 95%, and SOC_4 = 94%.

Figure 14 depicts the experimental results of the main circuit during operation. It is evident that the discharge of the battery cells follows a similar pattern as shown in Figure 11. Initially, cell1, which has the highest state of charge (SOC), discharges with the largest current, while the *SOC* values of the four cells gradually converge. The differences in current variation references are smaller compared to those shown in Figure 11, mainly because the initial SOC differences are smaller. However, due to the lower output current of the low-voltage load in this case, the balancing current flowing through the converter is limited. In Figure 14a, it can be observed that the discharge currents of the four cells are greater than 2 A, indicating that the battery cells can adequately power the main circuit. The portion of the battery cell discharge currents minus 2 A represents the equalizing current, which supplies power to the low-voltage load. This suggests that the discharge of the main circuit and the low-voltage load circuit can be treated as independent parts, simplifying the system design.

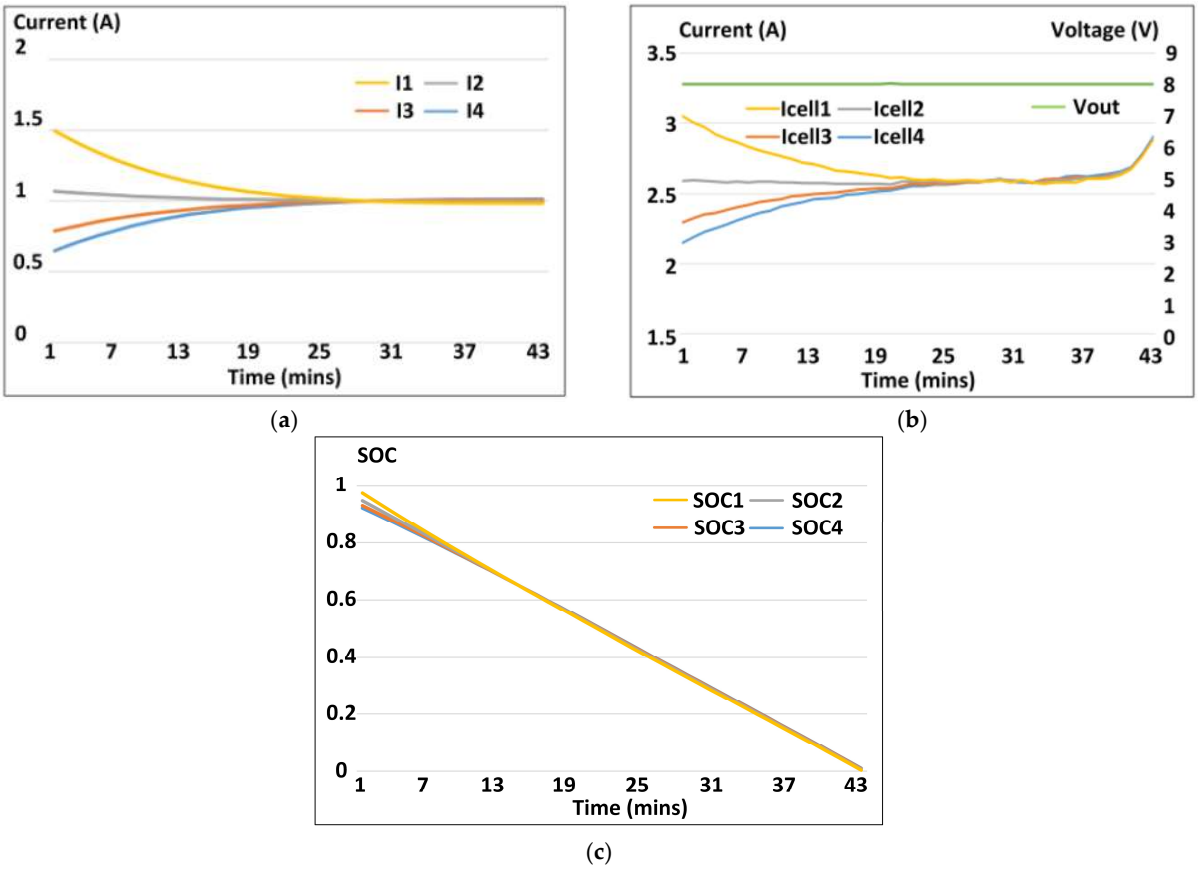

Figure 14. The sample experimental results when the main circuit works. (**a**) The current variation references of the four cells. (**b**) The discharging currents of the four cells and the output voltage of the converters. (**c**) The *SOC* values of the four cells.

In Figure 15, the battery system goes through several discharging and charging cycles. At t = 24 min, the first discharging cycle ends and the SOC of the battery cells is balanced, with a maximum difference of 0.85%. From t = 25 to 72 min, the four battery cells in series are charged with a constant current of 1.5 A, while maintaining a balanced state. At the end of the 72nd minute, cell1 is replaced with a fully charged cell, resulting in an SOC maximum difference of about 10%. From t = 73 to 109 min, the cells are discharged, with cell1 possessing the highest discharge current, while the other cells have similar discharge currents due to their close *SOC* values. At the end of the second discharging cycle, the

SOC of the cells is balanced with a maximum difference of 1.48%. After that, the series cells are charged again with a constant current of 2 A until the 140th minute, with the SOC differences remaining unchanged during this period. After t = 141 min, the cells continue to discharge and the SOC differences between them gradually decrease. Finally, at the end of the test, the maximum difference in SOC between all cells is approximately 0.23%, as shown in Figure 15a.

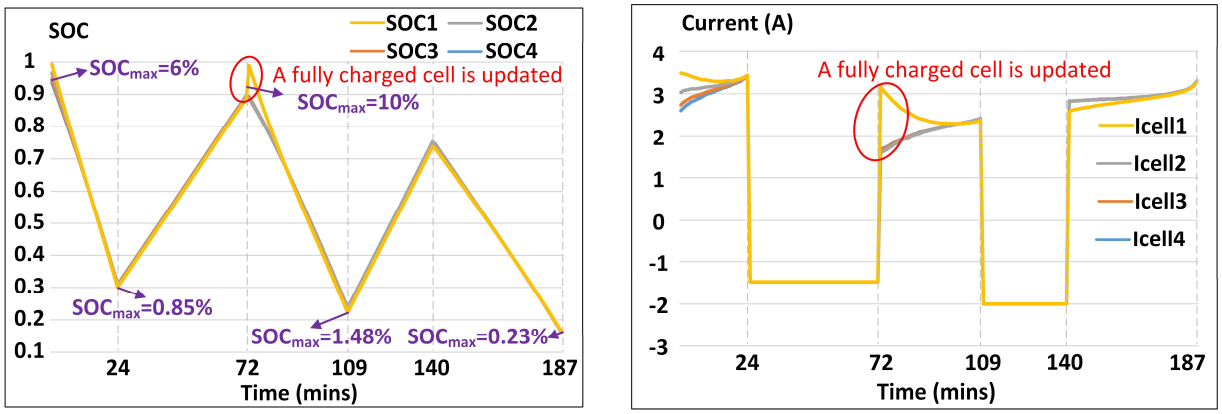

(**a**) (**b**)

Figure 15. The sample experimental results. (**a**) The *SOC* values of the four cells. (**b**) The discharging currents of the four cells.

6. Conclusions

The focus of this article is on the implementation of a dual-bus battery system architecture, which serves the dual function of SOC balancing and supplying power to low-voltage load. This is achieved without adversely affecting the normal operation of HV power rail and without needing additional balancing circuits or high step-down power converters, thus reducing the design complexity of the battery system. Unlike other balancing methods that rely solely on output regulation, the existing controller employs a current regulation approach that enhances output parallel capability and modularity, ensuring system stability and dynamics. Dynamic adjustment of the current variation references of the battery cells using the balancing algorithm effectively achieves SOC balancing.

The performance of the SOC balancing controller and system architecture proposed in this study is assessed and confirmed through experimentation using a four-cell battery system prototype. Under the presented balancing algorithm, the system can achieve balancing with an initial maximum SOC deviation of 12%, and the maximum difference at the end of discharging is only 0.7%. With the continuous operation of the balancing algorithm through multiple charge and discharge cycles, the maximum deviation can be reduced to 0.23%. Moreover, the maximum current difference between the batteries is as high as 1.7 A, which is much greater than the traditional passive balancing current (typically 100–200 mA); hence, the balancing speed is faster. The experiments demonstrate the successful achievement and maintenance of SOC balancing across the four cells, along with the provision of stable power to the low-voltage load, even during various discharging operations.

Author Contributions: Conceptualization, B.C. and D.Z.; methodology, X.W. and Y.W.; software, S.G.; validation, M.T. and S.C.; formal analysis, Y.D.; data curation, Y.C.; writing—original draft preparation, B.C. and F.L.; writing—review and editing, D.Z. and Y.C.; visualization, Y.C.; supervision, B.C.; project administration, Y.C.; funding acquisition, D.Z. All authors have read and agreed to the published version of the manuscript.

Funding: This research was funded by National Natural Science Foundation (NNSF) of China under Grant 62103443, by Hunan Natural Science Foundation under Grant 2022JJ40630, and by China Southern Power Grid Huizhou Power Supply Bureau R&D and innovation project under Grant

0313002023030301B200028. And the APC was funded by China Southern Power Grid Huizhou Power Supply Bureau R&D and innovation project.

Data Availability Statement: Data are contained within the article.

Acknowledgments: The authors of the paper would like to express their gratitude to Yingping Yuan for his help on the hardware implementation.

Conflicts of Interest: Daxing Zhang, Yankai Wang, Xiangdong Wang, Bingzi Cai, Shisen Gao, Mingming Tian, Suxiong Cai and Yuehui Den are employees of China Southern Power Grid Huizhou Power Supply Bureau, Yuan Cao and Feiliang Li are employees of Central South University. The paper reflects the views of the scientists, and not the company and university.

References

1. Yan, C.; Wang, C.; Hu, Y.; Yang, M.; Xie, H. Optimal operation strategies of multi-energy systems integrated with liquid air energy storage using information gap decision theory. *Int. J. Electr. Power Energy Syst.* **2021**, *132*, 107078. [CrossRef]
2. Alfraidi, W.; Shalaby, M.; Alaql, F. Modeling EV charging station loads considering on-road wireless charging capabilities. *World Electr. Veh. J.* **2023**, *14*, 313. [CrossRef]
3. Lee, K.B.; Ahmed, M.A.; Kang, D.K.; Kim, Y.C. Deep reinforcement learning based optimal route and charging station selection. *Energies* **2020**, *13*, 6255. [CrossRef]
4. Li, Y.; Han, M.; Yang, Z.; Li, G. Coordinating flexible demand response and renewable uncertainties for scheduling of community integrated energy systems with an electric vehicle charging station: A bi-level approach. *IEEE Trans. Sustain. Energy* **2021**, *12*, 2321–2331. [CrossRef]
5. Cao, Y.; Qahouq, J.A.A. Analysis and Evaluation of a Dual-Variable Closed-Loop Control of Power Converter with Wireless and Non-Wireless Power Transfer. *IEEE Trans. Ind. Electron.* **2019**, *6*, 2668–2679. [CrossRef]
6. Shi, J.; Gao, H.O. Efficient energy management of wireless charging roads with energy storage for coupled transportation–power systems. *Appl. Energy* **2022**, *323*, 119619. [CrossRef]
7. Liu, C.; Cai, X.; Chen, Q. Self-adaptation control of second-life battery energy storage system based on cascaded H-bridge converter. *IEEE Trans. Emerg. Sel. Top. Power Electron.* **2020**, *8*, 1428–1441. [CrossRef]
8. Huang, W.; Qahouq, J.A.A. Energy sharing control scheme for state-of-charge balancing of distributed battery energy storage system. *IEEE Trans. Ind. Electron.* **2015**, *62*, 2764–2776. [CrossRef]
9. Divakaran, A.; Minakshi, M.; Bahri, P.A.; Paul, S.; Kumari, P.; Divakaran, A.M.; Manjunatha, K.N. Rational design on materials for developing next generation lithium-ion secondary battery. *Prog. Solid State Chem.* **2021**, *62*, 100298. [CrossRef]
10. Alharbi, W.; Bhattacharya, K. Electric Vehicle Charging Facility as a Smart Energy Microhub. *IEEE Trans. Sustain. Energy* **2017**, *8*, 616–628. [CrossRef]
11. Liu, Z.; Wen, F.; Ledwich, G. Optimal planning of electric-vehicle charging stations in distribution systems. *IEEE Trans. Power Deliv.* **2013**, *28*, 102–110. [CrossRef]
12. Lindh, P.; Gerami Tehrani, M.; Lindh, T.; Montonen, J.H.; Pyrhönen, J.; Sopanen, J.T.; Niemelä, M.; Alexandrova, Y.; Immonen, P.; Aarniovuori, L.; et al. Multidisciplinary Design of a Permanent-Magnet Traction Motor for a Hybrid Bus Taking the Load Cycle into Account. *IEEE Trans. Ind. Elect.* **2016**, *63*, 3397–3408. [CrossRef]
13. Liu, W.; Tang, C.Y.; Wang, T.R.; Na, W.; Sun, J.L. Research on Active Equalization Topology and Control Strategy of Series Battery Pack. *J. Power Supply* **2020**, *33*, 682–690.
14. Hua, Y.; Zhou, S.D.; Cui, H.G.; Liu, X.H.; Zhang, C.; Xu, X.; Ling, H.P.; Yang, S.C. A comprehensive review on inconsistency and equalization technology of lithium-ion battery for electric vehicles. *Int. J. Energy Res.* **2020**, *44*, 11059–11087. [CrossRef]
15. Gao, M.Y.; Qu, J.F.; Lan, H.; Wu, Q.X.; Lin, H.P.; Dong, Z.K.; Zhang, W.Z. An Active and Passive Hybrid Battery Equalization Strategy Used in Group and between Groups. *Electronics* **2020**, *9*, 1744. [CrossRef]
16. Zhang, K.; Sun, L.; Fan, S.G. Research on design methodology of super capacitor balancing system based on multi-winding transformer. *Power Electron.* **2018**, *52*, 37–40. [CrossRef]
17. Diao, W.P.; Xue, N.N.; Bhattacharjee, V.; Jiang, J.C.; Karabasoglu, O.; Pecht, M. Active battery cell equalization based on residual available energy maximization. *Appl. Energy* **2018**, *210*, 690–698. [CrossRef]
18. Hicham, C.; Golbon, N.; Hmouz, I.; Souissi, R.; Tahar, S. Lyapunov-based adaptive state of charge and state of health estimation for lithium-ion batteries. *IEEE Trans. Ind. Electron.* **2015**, *62*, 1610–1618.
19. Chen, L.; Tian, B.; Lin, W.; Ji, B.; Li, J.; Pan, H.H. Analysis and prediction of the discharge characteristics of the lithium–ion battery based on the Grey system theory. *IET Power Electron.* **2015**, *8*, 2361–2369. [CrossRef]
20. Chen, G.W.; Liu, Z.T.; Su, H.; Zhuang, W.C. Electrochemical-distributed thermal coupled model-based state of charge estimation for cylindrical lithium-ion batteries. *Control Eng. Pract.* **2021**, *109*, 1006–1018. [CrossRef]
21. Gozdur, R.; Guzowski, B.; Dimitrova, Z.; Noury, A.; Mitukiewicz, G.; Batory, D. An energy balance evaluation in lithium-ion battery module under high temperature operation. *Energy Convers. Manag.* **2021**, *227*, 113565. [CrossRef]
22. Moon, S.; Kim, J. Balanced charging strategies for electric vehicles on power systems. *Appl. Energy* **2017**, *189*, 44–54. [CrossRef]

23. Turksoy, A.; Teke, A.; Alkaya, A. A comprehensive overview of the dc-dc converter-based battery charge balancing methods in electric vehicles. *Renew. Sustain. Energy Rev.* **2020**, *133*, 110274. [CrossRef]
24. Kim, M.Y.; Kim, C.H.; Kim, J.H.; Moon, G.W. A chain structure of switched capacitor for improved cell balancing speed of lithium-ion batteries. *IEEE Trans. Ind. Electron.* **2014**, *61*, 3989–3999. [CrossRef]
25. Hannan, M.A.; Hoque, M.M.; Peng, S.E.; Uddin, M.N. Lithium-ion battery charge equalization algorithm for electric vehicle applications. *IEEE Trans. Ind. Appl.* **2017**, *53*, 2541–2549. [CrossRef]
26. Kim, C.H.; Kim, M.Y.; Moon, G.W. A modularized charge equalizer using a battery monitoring IC for series-connected Li-ion battery strings in electric vehicles. *IEEE Trans. Power Electron.* **2013**, *28*, 3779–3787. [CrossRef]
27. Baughman, A.C.; Ferdowsi, M. Double-tiered switched-capacitor battery charge equalization technique. *IEEE Trans. Ind. Electron.* **2008**, *55*, 2277–2285. [CrossRef]
28. Hsieh, Y.H.; Liang, T.J.; Chen, S.M.O.; Horng, W.Y.; Chung, Y.Y. A novel high-efficiency compact-size low-cost balancing method for series-connected battery applications. *IEEE Trans. Power Electron.* **2013**, *28*, 5927–5939. [CrossRef]
29. Park, H.; Kim, C.; Kim, C.; Moon, G. A modularized charge equalizer for an HEV lithium-ion battery string. *IEEE Trans. Ind. Electron.* **2009**, *56*, 1464–1476. [CrossRef]
30. Riczu, C.; Bauman, J. Implementation and System-Level Modeling of a Hardware Efficient Cell Balancing Circuit for Electric Vehicle Range Extension. *IEEE Trans. Ind. Appl.* **2021**, *57*, 2883–2895. [CrossRef]
31. Raeber, M.; Heinzelmann, A.; Abdeslam, D.O. Analysis of an Active Charge Balancing Method Based on a Single Nonisolated DC/DC Converter. *IEEE Trans. Ind. Electron.* **2021**, *68*, 2257–2265. [CrossRef]
32. Ma, Y.; Duan, P.; Sun, Y.; Chen, H. Equalization of Lithium-Ion Battery Pack Based on Fuzzy Logic Control in Electric Vehicle. *IEEE Trans. Ind. Electron.* **2018**, *65*, 6762–6771. [CrossRef]
33. Chen, Y.; Liu, X.; Cui, Y.; Zou, J.; Yang, S. A MultiWinding Transformer Cell-to-Cell Active Equalization Method for Lithium-Ion Batteries with Reduced Number of Driving Circuits. *IEEE Trans. Power Electron.* **2016**, *31*, 4916–4929.
34. Mai, R.K.; Xu, B.; Yan, Z.T.; Zhou, W.; Liu, L.Z. A compact-size multi-winding transformer-based discharge equalizer for electric two-wheelers and three-wheelers vehicles power battery. *IEEE Trans. Veh. Technol.* **2022**, *71*, 4889–4897. [CrossRef]
35. Cao, Y.; Qahouq, J.A.A. Hierarchical SOC balancing controller for battery energy storage system. *IEEE Trans. Ind. Electron.* **2021**, *68*, 9386–9397. [CrossRef]
36. Evzelman, M.; Rehman, M.M.U.; Hathaway, K.; Costinett, R.; Zane, D.; Maksimovic, D. Active Balancing System for Electric Vehicles with Incorporated Low-Voltage Bus. *IEEE Trans. Power Electron.* **2016**, *31*, 7887–7895. [CrossRef]
37. Erickson, R.W.; Maksimović, D. *Fundamentals of Power Electronics*, 2nd ed.; Kluwer Academic Publishers: Norwell, MA, USA, 2001.